NANO LETTERS

Letter

pubs.acs.org/NanoLett

Excess Li-Ion Storage on Reconstructed Surfaces of Nanocrystals To Boost Battery Performance

Yandong Duan,[†] Bingkai Zhang,[†] Jiaxin Zheng,[†] Jiangtao Hu,[†] Jianguo Wen,[‡] Dean J. Miller,[‡] Pengfei Yan,[§] Tongchao Liu,[†] Hua Guo,[†] Wen Li,[†] Xiaohe Song,[†] Zengqing Zhuo,[†,∥] Chaokun Liu,[†] Hanting Tang,[†] Rui Tan,[†] Zonghai Chen,[‡] Yang Ren,[∥] Yuan Lin,[†] Wanli Yang,[⊥] Chong-Min Wang,[§] Lin-Wang Wang,[#] Jun Lu,[‡] Khalil Amine,[‡] and Feng Pan*[,†]

[†]School of Advanced Materials, Peking University, Shenzhen Graduate School, Shenzhen 518055, People's Republic of China

[‡]Center for Nanoscale Materials, [∥]X-ray Science Division, Argonne National Laboratory, Argonne, Illinois 60439, United States

[§]Environmental Molecular Sciences Laboratory, Pacific Northwest National Laboratory, 902 Battelle Boulevard, Richland, Washington 99352, United States

[⊥]Advanced Light Source, [#]Materials Science Division, Lawrence Berkeley National Laboratory, Berkeley, California 94720, United States

Supporting Information

ABSTRACT: Because of their enhanced kinetic properties, nanocrystallites have received much attention as potential electrode materials for energy storage. However, because of the large specific surface areas of nanocrystallites, they usually suffer from decreased energy density, cycling stability, and effective electrode capacity. In this work, we report a size-dependent excess capacity beyond theoretical value (170 mA h g^{-1}) by introducing extra lithium storage at the reconstructed surface in nanosized $LiFePO_4$ (LFP) cathode materials (186 and 207 mA h g^{-1} in samples with mean particle sizes of 83 and 42 nm, respectively). Moreover, this LFP composite also shows excellent cycling stability and high rate performance. Our multimodal experimental characterizations and ab initio calculations reveal that the surface extra lithium storage is mainly attributed to the charge passivation of Fe by the surface C−O−Fe bonds, which can enhance binding energy for surface lithium by compensating surface Fe truncated symmetry to create two types of extra positions for Li-ion storage at the reconstructed surfaces. Such surface reconstruction nanotechnology for excess Li-ion storage makes full use of the large specific surface area of the nanocrystallites, which can maintain the fast Li-ion transport and greatly enhance the capacity. This discovery and nanotechnology can be used for the design of high-capacity and efficient lithium ion batteries.

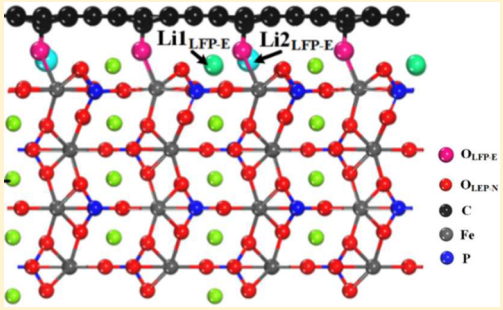

KEYWORDS: *Cathode materials, reconstructed surface, lithium-ion batteries, excess capacity, size-dependent*

The pressing demand for electric vehicles calls for lithium ion batteries (LIBs) with high capacity and high rate performance, which depends on the developments of high-performance cathodes based on both new materials and novel architecture. Recently, nanocrystallites have received much attention as promising electrode materials for energy storage.[1−3] Nanocrystallites benefit from the reduction of Li-ion diffusion path length, which enhances the kinetic properties in particles such as $LiMPO_4$ (M = Fe, Mn, Co). In particular, recent experiments have shown that nanometer-sized particles of $LiFePO_4$ (LFP), a commercially viable LIB cathode material, can achieve high-rate performance.[4−7]

However, compared with bulk materials, the employment of nanocrystallites in batteries suffers from several disadvantages. First, nanocrystallites have a large specific surface area, which is expected to decrease the capacity for lithium storage because of the reduced binding energy for surface lithium with its truncated symmetry. Ceder et al. calculated the surface potential for lithium storage on a LFP (010) surface, which is the main exposed surface, and found that it is lower than the bulk value by 0.6 eV.[8] It is also reported that nanometer-sized LFP particles exhibit sloping voltage charge/discharge curves, unlike the charge/discharge platform seen in larger LFP particles,[9] which leads to decreased voltage and thus energy density. Second, compared with bulk materials, the large specific surface area of nanocrystallites could lead to severe chemical activities due to the facilitated chemical catalysis,[10] which typically compromises electrolyte stability. Third, the large specific area of nanocrystallites enhances the infamous dissolution of transition-metal cations,[11] which jeopardizes the stability and cycling life of the battery. Fourth, nanosizing is

Received: June 1, 2017
Revised: August 1, 2017
Published: August 3, 2017

DOI: 10.1021/acs.nanolett.7b02315
Nano Lett. XXXX, XXX, XXX−XXX

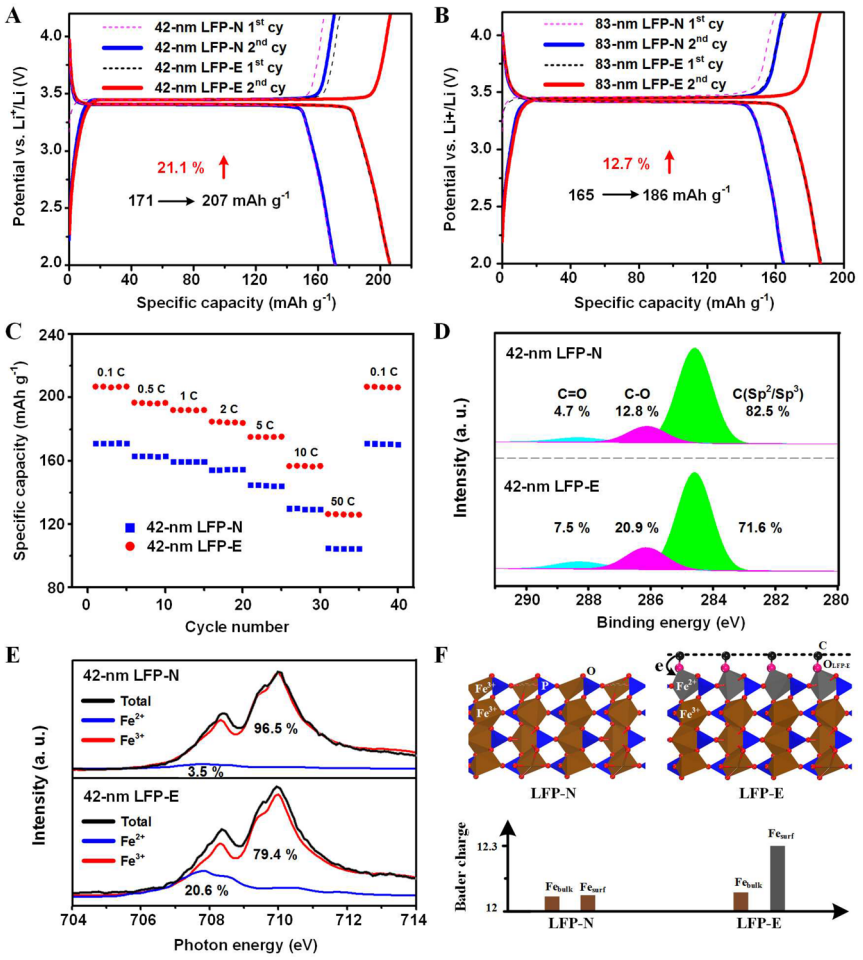

Figure 1. (A–B) Charge and discharge curves of LFP (N = Normal, E = Excess) composite samples. (C) Rate performance of various LFP composite samples. (D) XPS C 1s spectra of the LFP composite samples. The main peaks centered at 284.6 eV correspond to sp2/sp3 hybridized carbon atoms, and the independent peaks with energies of 285.6–286.2 eV and 288.4–288.7 eV can be assigned to carbon atoms in C–O and C═O groups, respectively. (E) Experimental XAS spectra (black lines) and Fe^{2+}/Fe^{3+} fitting spectra (colored lines) for two completely delithiated 42 nm LPF composite samples. (F) Bader charge of Fe atoms for charged LFP-N and LFP-E structures.

expected to reduce the tap density and further decrease the total energy density of an electrode.[12,13] Hence, the technical challenge on employing nanocrystallites for LIBs remains formidable, and new methodologies and nanotechnologies are required for truly utilizing the advantages of the nanocrystallites' fast Li-ion transport to achieve high power density, while using the ultrahigh surface area to store Li ions to enhance energy density and avoid side reactions with electrolytes for long-term stability.

Here we report a strategy of surface reconstruction that could mitigate the technical disadvantages of LFP nanocrystallites and advance the battery technology for high capacity and high rate performance. Through a special surface reconstruction, our LFP nanocrystallites show a size-dependent excess capacity, resulting in capacities of 186 and 207 mA h g^{-1} (beyond the theoretical value of 170 mA h g^{-1} by 9.4% and 21.8%, respectively) in samples with mean particle sizes of 83 and 42 nm, respectively. Moreover, composite electrodes based on such LFP nanocrystallites show a high cycling stability and high rate performance. After 1000 cycles at 10 C, the loss of capacity is only 0.3–1.1%, and at a 50 C rate, the electrodes still deliver capacities of 114 mA h g^{-1} and 127 mA h g^{-1} during charge and discharge, respectively. Our experimental tests and ab initio calculations demonstrated that the excess capacity comes from excess Li-ion storage at the reconstructed surface of LFP by C–O–Fe bonds, which can enhance binding energy for surface lithium by compensating surface Fe truncated symmetry to create two types of extra positions for Li-ion storage at the reconstructed surfaces. This phenomenon of excess capacity is also observed in $LiFe_{1-x}Mn_xPO_4$ ($0 \leq x \leq 1$) and $LiFe_{1-x}Co_xPO_4$ ($0 \leq x \leq 1$) materials. (The mechanism demo can be seen in details in Supplementary Movie 1.) The nanotechnology with the special carbon-coating process is applicable to large-scale production.

Results and Discussion. *Excess Capacity Observed by Electrochemical Experiments.* 42 and 83 nm LFP nanoparticles were synthesized by a reflux method. The obtained nanoparticles were single LFP phase as determined by X-ray diffraction (XRD) (Figure S1). Figure S2A shows a field-emission SEM image of the 42 nm LFP samples. It is clear that the LFP nanoparticles, which were produced by the reflux process, assume various shapes, like nanoplates, with an average size of 42 nm. The distribution of particle size was determined by analyzing SEM micrographs using an image analyzer (Nano measurer 1.2) with a total of at least 100 particles calculated on each image, and the results for 42 nm particles are shown in Figure S2B. The crystallinity and morphology characterization of 83 nm LFP nanoparticles is shown in Figure S2C–D.

DOI: 10.1021/acs.nanolett.7b02315
Nano Lett. XXXX, XXX, XXX–XXX

Excess LFP composite (designated LFP-E) was synthesized by mixing the as-prepared LFP with glucose solution and followed by grinding the mixture for 4 h at 40 °C. A corundum crucible containing the dried mixture was placed in a furnace under an Ar atmosphere and heated to 450 °C (at 2 °C/min), kept at 450 °C for 2 h, and then slowly heated to 650 °C (at 2 °C/min) and kept at 650 °C for 4 h. For comparison, a normal LFP composite (designated LFP-N) was also prepared, as follows: as-obtained LFP nanoparticles were dispersed into glucose solution by stirring, followed by drying and then heating at 650 °C for 10 h under an Ar atmosphere. Figure 1A−B shows the voltage curves of the LFP-E and LFP-N nanocomposites measured over 2.0−4.2 V at 0.1 C. Notably, the voltage platforms (which are a typical behavior of LFP) for the 83 and 42 nm LFP-E cathodes are longer, providing capacities from 186 to 207 mA h g^{-1}, which are higher than the capacities of 83 and 42 nm LFP-N cathodes and are beyond the theoretical value of 170 mA h g^{-1} for LFP. Meanwhile, these values are also much higher than the reported values of 120−168 mA h g^{-1} for commercially available or synthetic LFP materials.[13−18] Moreover, the 83 and 42 nm LFP-E cathodes also show high cycling stability and high rate performance; that is, after 1000 cycles at 10 C, the loss of capacity is only 0.3−1.1% (Figure S5), and at a 50 C charging and discharging rate, they still deliver capacities of 114 mA h g^{-1} and 127 mA h g^{-1} (Figure 1C and S6), respectively.

To further validate the excess capacity for the LFP-E, we did a prelithiation test on fresh samples of both LFP-E and LFP-N (Figure S8). We can see that after prelithiation to 2.0 V, the LFP-E gain more excess capacity (about 25 and 20 mA h g^{-1} for 42 and 83 nm samples, respectively) than the LFP-N (about 7.5 and 5 mA h g^{-1} for 42 and 83 nm samples, respectively). These excess capacities obtained upon prelithiation are also close to the excess capacities obtained from above normal electrochemical cycling. So where does the excess capacity come from? The only difference between LFP-E and LFP-N is the post-treatment of the LFP to produce LFP-E, as discussed in the Preparation Section. The most probable reason is the different LFP/carbon interface, as the grinding with glucose could lead to surface reconstruction of LFP. This excess capacity is different from that observed in recent work by Hu et al.,[19] who reported that the incorporation of LFP with few-layer graphene can deliver a capacity of 208 mA h g^{-1}, which is beyond the theoretical capacity of LFP (170 mA h g^{-1}). They attributed this excess capacity to the reversible reduction−oxidation reaction between the Li ions and the exfoliated graphene flakes. However, this mechanism lacks adequate experimental or theoretical support, and the cycling stability and rate capability are in general: the capacity is retained around 80 mA h g^{-1} at a current density of 28 C, and they only give the cycle life of 180 cycles. Moreover, the modifying process used is not applicable to large-scale production.

Experimental Tests To Find the Differences between the LFP-N and LFP-E. To clarify the mechanism of the excess capacity of LFP-E, we try to find the differences between the structure of LFP-E and LFP-N. High-resolution transmission electron microscopy (HRTEM) is first employed to observe the structure and microscopic morphology of the LFP-E and LFP-N samples (Figure S10). It clearly shows LFP nanoparticles wrapped within 2 nm thick amorphous carbon shells and is found that the carbon coating on LFP for LFP-E is denser than that for LFP-N and exhibits some layered structures.

X-ray photoelectron spectroscopy (XPS) is next performed on the carbon-coated LFP particles to analyze the elemental composition and chemical bonding configurations (Figure 1D and S11). The dominant carbon-containing functional groups at the LFP/carbon surface are C−C, C−O, and carbonyls (C═O). The XPS peak areas of each chemical bond were used to estimate the amount of each species on the surface (Table S4). In the XPS spectrum of the C−O group (Figure 1D and S11), the peaks for the 42 nm LFP-E and 83 nm LFP-E had higher intensities than those for the 42 nm LFP-N and 83 nm LFP-N. Here we propose that the larger content of C−O groups in LFP-E comes from the C−O−Fe bonds at the LFP/carbon interface, which can be maintained without reduction during carbon coating at around 500 °C under an $Ar/H_2(5\%)$ atmosphere. This hypothesis is reasonable, given that there are unpassivated Fe and Li atoms at the surface of LFP.[6] When LFP is placed in contact with glucose solution for grinding, the hydroxyl groups of the glucose molecules are expected to chemically bond with the unpassivated Fe atoms at the surface, through which the broken FeO_6 octahedral could be reconstructed similarly to the structure in the bulk. With the grinding and subsequent heating at 650 °C, the glucose molecules will be carbonized to amorphous carbon layers on the surface of the LFP. Because of the C−O−Fe bonding involving the FeO_6 octahedral at the reconstructed surface, the C−O groups at the interface should not be easily stripped during the grinding and high-temperature heating process, thus leading to excess C−O groups and denser carbon coating (Figure S10) compared with the LFP-N. As a result, there is a reconstruction of the LFP surface, which is chemically bonded with Fe−O−C carbon layers formed by the carbonized glucose, and the excess capacity may come from the excess Li storage sites at the reconstructed LFP surfaces.

The surface reconstruction model for the LFP-E is first supported by our cyclic voltammogram (CV) measurement of a single-particle (SP) electrode of LFP and the related numerical analysis (CV fitting in Methods). Compared with the LFP-N sample, the position of the CV peak of LFP-E is at a higher potential. This phenomenon is similar to our previous finding that the position of the CV peak of LFP in organic electrolyte is higher than that in aqueous electrolyte, which we attributed to the different surface reconstruction of the LFP surface in different electrolytes.[6] Here, the CV tests for both LFP-N and LFP-E are conducted in the same aqueous electrolyte, and the sizes of the LFP-N and LFP-E particles are also the same, so the different positions of the CV peak can be attributed to the different reconstructed LFP surfaces (see more details in CV fitting in Methods).

To further analyze the Fe evolution on the reconstructed surface, we employed synchrotron-based soft X-ray adsorption spectroscopy (sXAS) for a quantitative and comparative analysis of the surface Fe valences of both the LFP-N and LFP-E samples. sXAS has been demonstrated to be a powerful probe for quantitative analysis of 3d transition-metal valences in battery materials.[20,21] While sXAS could be collected with both bulk and surface sensitivity,[22] here we focus on the surface-sensitive total electron yield (TEY) signal of sXAS with a probe depth of about 10 nm. For both the lithiated pristine LFP-N and LFP-E samples, the Fe-L_3 sXAS, corresponding to the excitations of $2p^{3/2}$ core electrons to the 3d unoccupied states, displays the typical Fe^{2+} spectra,[20] as shown in Figures S14−17. However, the delithiated LFP-E sample shows a relatively higher intensity on the low energy (708.5 eV) shoulder

DOI: 10.1021/acs.nanolett.7b02315
Nano Lett. XXXX, XXX, XXX−XXX

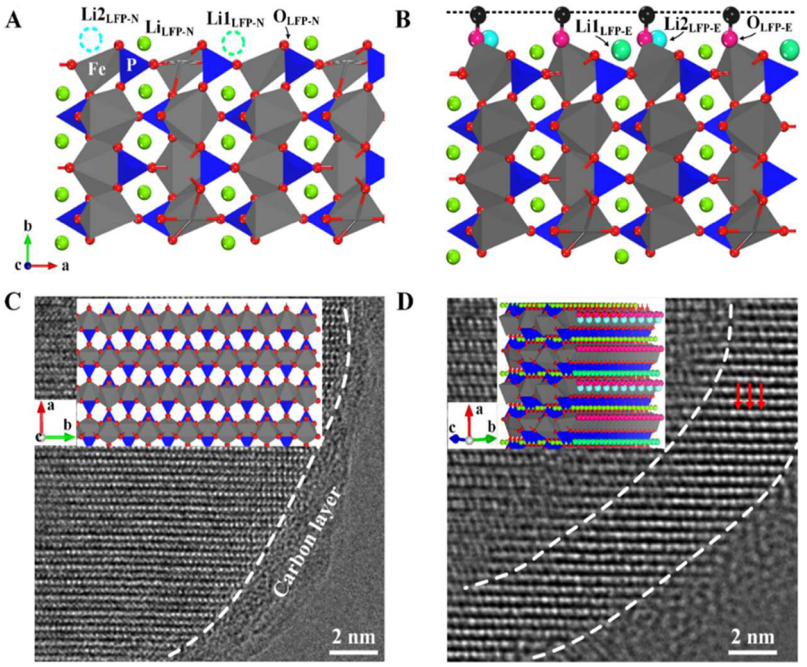

Figure 2. (A–B) Lithium and electron transfer and intercalation sites of excess Li atoms in the LFP-N and LFP-E structure, respectively. (C and D) Transmission electron micrograph of charged and discharged 42 nm LFP-E nanoparticles, respectively.

compared with that of LFP-N. The quantitative analysis of the Fe valence distribution[20] reveals that there is about 20% of Fe^{2+} in the LFP-E sample, contrasting the dominating Fe^{3+} of LFP-N (Figure 1E). The finding of the surface Fe^{2+} of the LFP-E sample is counterintuitive and nontrivial. Naively, the relatively higher capacity of the LFP-E electrode should correspond to higher Fe^{3+}, not Fe^{2+}, concentration at its delithiated (oxidized) state. On the contrary, our data in Figure 1E show that, while the overall line shape of the delithiated samples is consistent with the typical Fe^{3+} spectra,[20] there is a subtle increase of the Fe^{2+} concentration of the high capacity LFP-E sample. The small contrast is expected because, even with the 10 nm surface probe depth, the top surface layer contributes to only a small portion of the sXAS signal. Therefore, the sXAS data indicate that the Fe on the surface of the LFP-E sample is of bivalence.

Ab Initio Calculations To Verify the Proposed Surface Reconstruction Model. To clarify the surface reconstruction model and explain the above XAS observations, we employed ab initio calculations and a simple interface model of LFP surface reconstructed with Fe–O–C bonds covered by graphene (designated LFP/GP) for further study, which may shed some light on the origin of the excess capacity. The interface was built on the LFP (010) surface, since it is the most exposed surface and is normal to the Li diffusion channel within bulk LFP.[8] To maintain stoichiometric ratio and reduce the dipole moment, one Li vacancy reappears near every FeO_5 at the surface along the direction of Li diffusion channel. This, in effect, creates 50% Li vacancies in the outermost surface layer of LFP (010). The selected interface model is shown in Figure S18, and more detailed information about the interface model can be found in the SI. The two parts of the interface are connected by stable C–O–Fe bonds, as evident from the XPS results (Figure 1D).

Figure 2A–B shows all the sites considered for Li storages at the surfaces of LFP (010) and LFP/GP structures: $Li_{LFP\text{-}N}$ and $Li1_{LFP\text{-}N}$ sites denote the original Li storage sites and the Li vacancies near every FeO_5 on LFP (010) surfaces along the direction of Li diffusion channel, respectively. $Li1_{LFP\text{-}E}$ and $Li2_{LFP\text{-}E}$ sites denote our proposed extra Li storage sites at the LFP/GP interface [$Li1_{LFP\text{-}E}$ sites corresponds to the Li vacancies near every FeO_5 (or Li diffusion channel) on LFP (010) surfaces, and $Li2_{LFP\text{-}E}$ sites are between two oxygen atoms of C–O–Fe group]. $Li2_{LFP\text{-}N}$ sites in Figure 2A correspond to $Li2_{LFP\text{-}E}$ sites at the surface of LFP/GP structure in Figure 2B. The voltages of Li at different sites are shown in Table S6. Compared with LFP (010), the LFP/GP structure show three significant changes: (1) For LFP (010) surface, the intercalation voltage at $Li_{LFP\text{-}N}$ sites is 2.79 V, which is lower than that in the bulk value (3.45 V) and close to the previous reports.[8] The lower voltage can be attributed to the weaker bonding environment at the surface for Li ions[8] But for LFP/GP, the intercalation voltage at $Li_{LFP\text{-}N}$ sites is 3.02 V. (2) For LFP (010) surface, the intercalation voltage of $Li1_{LFP\text{-}N}$ sites is −0.13 V, suggesting an unfavorable thermodynamic state. But for LFP/GP, the intercalation voltage of $Li1_{LFP\text{-}E}$ sites is 3.01 V. (3) For LFP (010) surface, the intercalation voltage of $Li2_{LFP\text{-}N}$ sites is −0.25 V. But for LFP/GP, the intercalation voltage of $Li2_{LFP\text{-}E}$ sites is 2.68 V.

This is because the original (010) surface of LFP is already self-passivated for charge compensation to satisfy the electron counting rule; there is no excess dangling O to bond with excess Li at the $Li1_{LFP\text{-}N}$ site, thus leading to the low binding energy for the excess Li atom storage. By contrast, at the LFP/GP interface, the dangling Fe and Li bond with the C–O–Fe groups instead of the original dangling O bonds at the surface. As a result, these surface dangling O atoms would bond with excess Li at the $Li1_{LFP\text{-}E}$ site more strongly, thus leading to high binding energy. Meanwhile, compared with the three-coordinated Li atom at the LFP (010) surface, the Li atoms at the reconstructed LFP-E surface are four-coordinated because of the C–O–Fe groups, which also helps increase the binding energy of Li atoms at the surfaces. Besides, the oxygen of C–O–Fe group can also bond extra Li atoms at the $Li2_{LFP\text{-}E}$ sites to form −COLi for extra Li storage. Thus, we can

DOI: 10.1021/acs.nanolett.7b02315
Nano Lett. XXXX, XXX, XXX–XXX

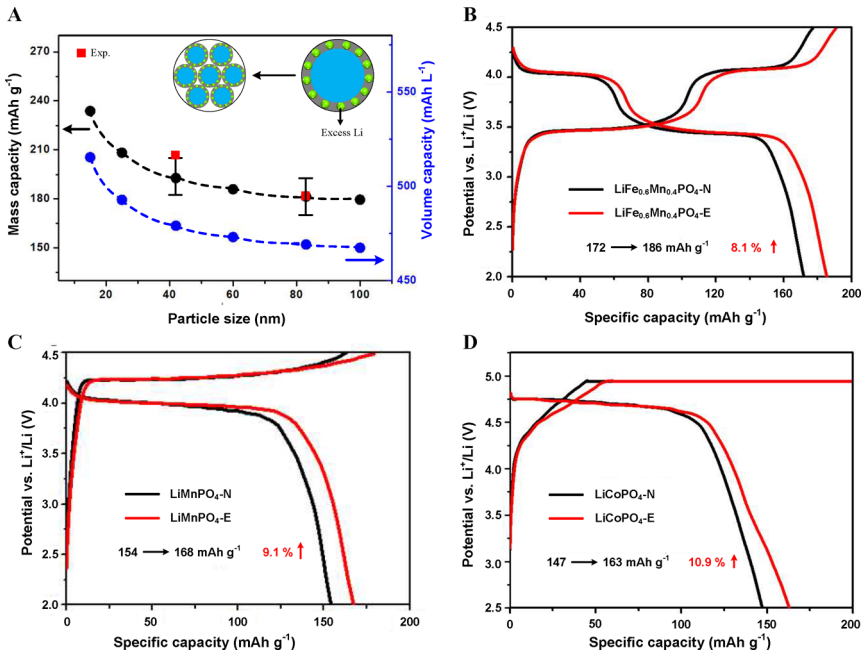

Figure 3. (A) Experimental and theoretical size-dependent excess capacity in LFP. Calculated mass capacity of LFP-E (black circles) as a function of particle size, experimental values (red squares), and volume capacity as a function of particle size (blue circles). Error bars correspond to standard deviations. The dashed red line corresponds to the VC trends of LFP-N. (B–D) Charge and discharge curves of $LiFe_{0.6}Mn_{0.4}PO_4$, $LiMnPO_4$, and $LiCoPO_4$ composite samples, respectively.

deduce that decreasing the particle size would lead to larger excess capacity due to the increased surface area.

Above surface reconstruction model for excess Li-ion storage was consistently supported by the formation of the superstructures at the particle surface region as revealed by HRTEM observation of surface structures of the normal LFP, delithiated, and lithiated LFP-E (Figure 2C–D and S24–S27). Apparently, near the surface of the grain for the lithiated LFP, some superstructures are observed. In the surface layer, more double unit-cell dots are observed compared to a uniform intensity inside the grain (Figure 2C). By contrast, for LFP-N and delithiated LFP-E, no obvious surface superstructure is observed (Figures S24–S25).

Furthermore, Bader charge analysis and the calculation of excitation energies of Fe atoms were used to validate the interface model. The Bader charge of Fe atoms at the surface (Fe_{surf}) and in the bulk (Fe_{bulk}) for different systems is shown in Figure 1F. It was found that the charge of Fe_{surf} in $FePO_4$/GP is 12.300, which is between 12.537 (the value for Fe^{2+}) and 12.065 (the value for Fe^{3+}), suggesting that the Fe_{surf} in $FePO_4$/GP is about $Fe^{2.5+}$ and different from the Fe_{surf} at the LFP (010) surface, which is Fe^{3+}. Then, the $FePO_4$/GP system energies with Fe_{surf} and Fe_{bulk} atom electronic excitation were calculated. It was found that the total-energy difference between the two states is about 1.6 eV, indicating two different valence states of Fe atoms. It is known that the valence state of Fe_{bulk} is 3+ in the $FePO_4$/GP system. Thus, this difference suggests that the valence state of Fe_{surf} is lower than 3+. Fe L-edge XAS spectra of LFP and $FePO_4$, involving the excitation of Fe 2p core electrons to the empty 3d orbitals, were obtained, and the photon energy difference between Fe^{2+} (LFP) and Fe^{3+} was about 2 eV.[6,7] A comparison of the energy difference between experimental (2.0 eV) and theoretical (1.6 eV) results indicates that the valence state of Fe_{surf} in $FePO_4$/GP should be between 2+ and 3+, which is consistent with the Bader analysis. Considering the possible complication of the real reconstructed surface structures of LFP-E and the accuracy of the density functional theory (DFT) method, these results agree with XAS measurements showing that the surface Fe atoms partially remain in the Fe^{2+} state. These consistent findings lead to a microscopic scenario: when the Li ions are fully extracted, the C–O–Fe can transfer electrons to the Fe atoms at the surface to prevent them from being oxidized to Fe^{3+}. By contrast, all Fe^{2+} ions are oxidized to Fe^{3+} in the LFP-N.

Beyond this simple LFP/GP interface model, we also considered the voltage of Li at the excess sites for a series of LFP/carbon interfaces with C–O–Fe bonds (Figure S20). Interestingly, we found that not all structures with C–O–Fe bonds exhibit high Li voltage. Some interface structures have about 2.6 V or even lower for excess-Li storage sites. Some interface structures have high voltage, up to almost 3.5 V, for excess-Li sites. We suggest that the sensitivity of Li voltage to the interface C–O–Fe structure can be related to the hybridization type of the C contacting the LFP surface. If the C has four hybrid orbitals (i.e., sp^3), the interface will show high Li voltage.

On the other hand, if the C has three hybrid orbitals (i.e., sp^2), the interface will show low Li voltage because some electrons are pulled away by the sp^2 C with the π-electron coupling. This is because under sp^3 hybridization, more p orbitals of the O atom at the end of C will bond with the surface Fe and Li atoms, thus leading to better charge passivation for the truncated surface and stronger coordination for the surface Li atoms.

Strategy Applied to Other Cathode Materials with Nanocrystals. Figure 3A summarizes the experimental and theoretical size-dependent excess capacity in LFP. We can see an increase in excess capacity with reduced particle size, which can be attributed to the increased specific area for excess-Li storage. If there is no extra lithium storage at the surface, the

DOI: 10.1021/acs.nanolett.7b02315
Nano Lett. XXXX, XXX, XXX–XXX

volume capacity of LFP-N would decrease with the decreasing particle size due to the increasing surface areas which would degrade and even make the advantages of nanoparticles useless. However, the volume capacity of LFP-E shows a favorable trend as shown in Figure 3A, where it is seen that volume capacity of LFP-E increases with decreasing particle size. This result indicates that excess Li at the surface of LFP-E contributes significantly to the volume capacity performance. Finally, to examine whether this surface reconstruction for excess-Li storage can be applied to other cathode materials, we have prepared carbon-coated $LiMPO_4$ (M = Fe, Mn, and Co) composites and calculated Li intercalation voltages for $LiMnPO_4$/GP, $LiCoPO_4$/GP, $LiFe_{0.5}Mn_{0.5}PO_4$/GP, and $LiFe_{0.5}Co_{0.5}PO_4$/GP using similar hybrid interface models. The charge and discharge curves (Figure 3B–D) show that $LiMPO_4$-E composites provide higher capacity compared to their normal counterparts. Meanwhile, the calculated intercalation voltages of excess Li (see Table S6) show that like LFP/GP, the $LiMnPO_4$/GP, $LiCoPO_4$/GP, $LiFe_{0.5}Mn_{0.5}PO_4$/GP, and $LiFe_{0.5}Co_{0.5}PO_4$/GP also exhibit a high intercalation voltage for excess Li compared with LFP (010) surfaces. It is observed that the C–O–M (M = Fe, Mn, and Co) structure, as a simple geometrical descriptor, can be utilized to rationalize the experimental debate about the excess Li on carbon-coated $LiMPO_4$ (M = Fe, Mn, and Co) composites.

Conclusion. In summary, by combination of experiment and theoretical calculation, we revealed an excess-Li storage capacity at the reconstructed surface in nanosized $LiFePO_4$. This discovery can be used for the design of high-capacity and efficient LIBs. It would be easy to achieve excess capacity for LIBs by fully using the large surface areas of nanosized particles, to reconstruct the $LiMPO_4$ surface by passivating the surface M cations via introducing stable X-–Y (e. g., O or N) –M structure with a sp^3 hybridization type and making surface unsaturated oxygen atoms bond with more Li for extra lithium storage.

Experimental Section. *Synthesis of LFP, $LiMPO_4$, and $LiFeMPO_4$ (M = Mn and Co; $LiMnPO_4$ Is Denoted as LMP and $LiCoPO_4$ Is Denoted as LCP).* 42 nm LFP nanoparticles were synthesized by a reflux method. First, 1.39 g of $FeSO_4{\cdot}7H_2O$ was dissolved in 50 mL of ethylene glycol with stirring. Meanwhile, 0.566 g of $LiOH{\cdot}H_2O$ was dissolved in 50 mL of ethylene glycol, followed by adding 0.735 g of H_3PO_4 to form a well-distributed solution. Subsequently, $FeSO_4{\cdot}7H_2O$ solution was introduced into the $LiOH{\cdot}H_2O$–H_3PO_4 mixed solution with dropwise addition under continuous magnetic stirring. After homogenization, the reaction mixture was heated under reflux conditions for 4 h under an Ar atmosphere and then naturally cooled to room temperature. The as-obtained precipitate was filtered, washed with deionized water and ethanol several times, and dried at 80 °C in a vacuum for 10 h. To prepare $LiMPO_4$ (M = Mn and Co), $MnSO_4{\cdot}H_2O$ or $CoSO_4{\cdot}7H_2O$ was introduced into the $LiOH{\cdot}H_2O$–H_3PO_4 mixed solution to start the reflux reaction. To prepare $LiFeMPO_4$/C (M = Mn and Co), stoichiometric amounts of $FeSO_4{\cdot}7H_2O$ and $MnSO_4{\cdot}H_2O$ solution, or $FeSO_4{\cdot}7H_2O$ and $CoSO_4{\cdot}7H_2O$ solution, were introduced into the $LiOH{\cdot}H_2O$–H_3PO_4 mixed solution to start the reflux reaction.

To prepare LFP nanoparticles with a mean size of 83 nm, the feeding sequence was changed. In this case, H_3PO_4 was slowly added to the $FeSO_4$ solution under stirring. Then LiOH solution was introduced into the mixture. Other steps were the same as for 42 nm LFP nanoparticles.

Preparation of LFP, $LiMPO_4$, and $LiFeMPO_4$ (M = Mn and Co) Composite Nanoparticles. To prepare the normal (N) LFP, $LiMPO_4$, and $LiFeMPO_4$ composites, the as-obtained LFP, $LiMPO_4$, and $LiFeMPO_4$ nanoparticles were dispersed into glucose solution (0.2 g of glucose in 10 mL of water) by stirring, followed by drying and then heating at 650 °C constantly for 10 h under an Ar atmosphere. Excess (E) LFP, $LiMPO_4$, and $LiFeMPO_4$ composites were synthesized by mixing the as-prepared LFP, $LiMPO_4$, and $LiFeMPO_4$ with glucose solution (0.2 g of glucose in 5 mL of mixed solvent, $V_{water}/V_{ethonal}$ = 1:1) by grinding for 4 h at 40 °C. A corundum crucible containing the dried mixture was placed in a furnace under an Ar atmosphere and was slowly heated to 450 °C (at 2 °C/min), kept at 450 °C for 2 h, and then slowly heated to 650 °C (at 2 °C/min) and kept at 650 °C for 4 h.

Structural Characterization. X-ray diffraction (XRD) measurements were carried out by using a Bruker D8 Advance diffractometer with a Cu-Ka radiation source. Rietveld refinements were performed to determine the lattice parameters and crystal size for the synthesized samples using the TOPAS 4.2 package. SEM (ZEISS Supra 55) was used to investigate the morphology and crystal structure of the as-synthesized samples. Inductively coupled plasma optical emission spectrometry (ICP-AES, JY2000-2, Horiba Jobin Yvon) measurement was performed to detect the element content of the prepared materials. The structural variations of the carbon layer in the composites were identified by Raman spectroscopy (iHR 320, Horiba Jobin Yvon, 532.1 nm laser). The specific surface area was analyzed by Brunauer–Emmett–Teller (BET) nitrogen adsorption–desorption measurement (Micromeritics, ASAP 2020 HD88). Distribution of particle size was determined by analyzing SEM micrographs using an image analyzer (Nano measurer 1.2), with a total of at least 100 particles calculated in each image.

Electrochemical Measurements for Coin-Type Cell. Electrochemical measurements were performed using CR2032-type cells assembled in an argon-filled glovebox. The electrode-supported normal/excess LFP, $LiMPO_4$, and $LiFeMPO_4$ (X = Mn, Co) nanoparticles were prepared according to the following steps: LFP, $LiMPO_4$, and $LiFeMPO_4$ (X = Mn, Co) composites were mixed with polyvinylidene fluoride binder and acetylene black carbon additive in a weight ratio of 7:2:1 and then dispersed in *N*-methylpyrrolidone. The slurries were pressed onto the aluminum foil current collector as working electrodes and dried at 120 °C in vacuum for 10 h. Lithium foils were used as the counter-electrodes. The active-material content in the electrode was around 1.0 mg. The charge/discharge performance of the coin cells was measured between 2.0 and 4.2 V at room temperature.

XPS Tests. The C–O bond for various samples was detected by XPS (ESCALab220I-XL) measurements, which were extra equipped with the ion etching system, domain XPS, and ion diffraction analysis system. This system used a focused monochromatic Al K α X-ray (1486.7 eV) source for excitation and a spherical section analyzer. All of the spectra were charge referenced using the C 1s line at 284.6 eV for comparison purposes.

Single-Particle (SP) Model and Cyclic Voltammogram (CV) Simulations. CV tests were carried out in 1 M $LiClO_4$ organic electrolyte (a mixture of ethylene carbonate and dimethyl carbonate, v/v = 1:1) at room temperature using a CHI 660e electrochemical workstation. Silver/silver chloride (Ag/AgCl) was used as the reference electrode, Pt wire as the counter-

DOI: 10.1021/acs.nanolett.7b02315
Nano Lett. XXXX, XXX, XXX–XXX

electrode, and a gold disk electrode with various cathode materials as the working electrode. To prepare the working electrode, 10 mg of as-synthesized normal or excess LFP composites were mixed with 3 mg of acetylene black, 150 μL of Nafion solution (5.0% Nafion in ethanol), and 1 mL of *N*-methyl pyrrolidone. The mixture was sonicated for 2 h, and a very little amount of the suspension was applied onto a gold disk electrode and then fully dried.

A SP model of LFP has been developed by us to measure performance and collect a single-particle LFP nanocrystal's intrinsic properties for Li-ion batteries. We model the LFP active material as separate nanosized spheres—in which the Li ions diffuse along the *b*-axis-that are coated onto the electrode evenly to form an ultrathin SP electrode.[23]

Through fitting the sharp CV peaks of the SP electrode by a binary system model (Figure S13), we find that the intrinsic Li-ion diffusion coefficients of LFP are nearly the same for the LFP-E and LFP-N (Table S5), but the surface reaction coefficient for LFP-N is two times higher than that for LFP-E. In our previous work, we reported that a solvation/desolvation occurs for the surface Li in the charge/discharge process. Because of the surface reconstruction of the LFP-E due to the C−O−Fe bonds, the graphene-like carbon layers are in close contact with the surface LFP, which is expected to prevent contact between the solvent molecules and the surface Li. Thus, the surface Li ions have to diffuse along the surface to the cavern places of the graphene-like carbon layers, where they are solvated by the electrolyte molecules. This process would slow the surface reaction, thus leading to a lower surface reaction coefficient than that of LFP-N.

Soft X-ray Absorption Spectroscopy (XAS) and Simulation. Fe L-edge, C K-edge, and O K-edge XAS was performed at the undulator beamline 8.0 of the Advanced Light Source at Lawrence Berkeley National Laboratory. The beamline is equipped with a spherical grating monochromator and supplies linearly polarized soft X-rays with resolving power up to 6000. The spectra were collected in both total electron yield (TEY) and total fluorescence yield (TFY) modes, with probe depths of about 10 and 100 nm, respectively. All data were normalized to the photon flux of the incident beam.

For the quantitative Fe valence distribution analysis, we construct the simulated spectra by linear combinations of the spectra of the two end states, that is, the spectra of the Fe L-edge of $LiFePO_4$ and $FePO_4$ that were collected on reference samples of uncoated $LiFePO_4$ with full chemical delithiation. This method based on sXAS has been successfully demonstrated in various 3d transition-metal battery compounds.[20]

High-Resolution Transmission Electron Microscopy (HRTEM). Scanning/transmission electron microscopy (S/TEM) (a JEOL JEM-2100F FEG FasTEM with an accelerating voltage of 200 kV) was employed to evaluate the samples. HRTEM was carried out using the Argonne chromatic aberration-corrected TEM (ACAT), a FEI Titan 80-300 with an image corrector to correct spherical and chromatic aberration to achieve resolution better than 0.08 nm at 200 kV. To prepare the TEM specimens, a dilute suspension was prepared by ultrasonically dispersing the samples in ethanol for 5 min, and a drop of the suspension was placed onto a copper grid and dried.

Computational Details. All ab initio calculations were performed using the Vienna ab initio simulation package[24] with the projector augmented wave pseudopotentials[25] and the generalized gradient approximation exchange-correlation function developed by Perdew, Burke, and Ernzerhof.[26] The structural relaxation simulation used the conjugated gradient minimization method with a maximum force tolerance on each atom of 0.02 eV/Å. DFT + U correction was used for all LMP composites (M = Fe, Mn, and Co). The values of U were set at 5.3, 4.5, and 5.8 eV for Fe, Mn, and Co, respectively. The plane wave cutoff was set at 500 eV, and the k-point mesh in the Monkhorst−Pack scheme was set at 2 × 2 × 1. The average intercalation voltages for Li_xFePO_4, Li_xMnPO_4, and Li_xCoPO_4 are calculated to be 3.46, 4.03, and 4.64 V at the range of $0 \leq x \leq 1$, which are consistent with experimental values (3.5,[19] 4.1,[27] and 4.8 V,[27]) respectively.

The establishment of a synergistic model is the first step in studying electronic structural changes and lithium intercalation in the LFP/GP interface. The (010) surface of LFP is the most thermodynamically stable one, which favors the Li diffusion in a one-dimensional pathway. Therefore, a four−O−P−O-layer LFP (010) surface was used as a support with a 2 × 1 (9.48 × 10.47 Å^2) unit cell. A 3 × 3 GP unit (9.84 × 12.28 Å^2 in size) was placed on the O-terminated surface of LFP (010), as shown in Figure S18A−B. After binding-energy (i.e., $E_b = E_{graphene} + E_{LiFePO4} - E_{LiFePO4/graphene}$) calculations, it was found that the binding energies of GP are 3.06 and 0.15 eV for O1- and O2-terminated surfaces, respectively. The strong interaction between GP and LFP could prevent the agglomeration of LFP nanoparticles. The C−O bonds are formed in the LFP/GP interface when GP is adsorbed on the O1-terminated surface (Figure S18C), and the detailed interface parameters (bond lengths, angle, and charge distribution of the C−O bond) are shown in Figure S18D. The C−O bond is evident from the XPS spectra shown in Figure S11. Therefore, the former interface structure shown in Figure S18C is chosen as the structure used in the subsequent calculations because it is more persuasive for describing the experimental situation. In the LFP/GP structure, the distance between the LFP surface and the GP is 2.76 Å, and the bond distances of C−O and O−Fe are 1.48 and 1.98 Å, respectively. GP in the structure remains flat (except for C atoms with C−O bonds, whose sites are sunken). Similarly, the $LiMnPO_4$/GP, $LiFeMnPO_4$/GP, and $LiFeCoPO_4$/GP hybrid models were built in the same way.

Excess Capacity of LFP/GP with Different Particle Sizes. On the basis of the interface structure (Figure S19) and calculated storage voltage (Table S6), there are four excess Li atoms in one supercell. Next, we will evaluate the excess capacity of LFP/GP with different particle sizes. With one mole LFP selected as a reference, the relationship among different variables, such as volume (V) and surface area (S) of the (010) surface of each particle, the mass density of LFP (ρ_{LFP}), the number of the LFP (n, n meaning the number of bulk cell LFP), s the molar mass of LFP, the surface area of one supercell (S'), the total mass of excess Li atoms intercalated onto the (010) surface (m_{Li}), and the Avogadro constant (N_A), can be defined by eqs 1−3:

$$V\rho_{LFP}n = M_{LFP} \tag{1}$$

$$4\frac{S}{S'}n = m_{Li} \times \frac{N_A}{M_{Li}} \qquad S' = ac \tag{2}$$

$$\rho_{LFP} = 8M_{LFP}/(N_A V') \qquad V' = abc \tag{3}$$

Then we can derive the mass (m_{Li}) of excess Li for every molar LFP, that is,

DOI: 10.1021/acs.nanolett.7b02315
Nano Lett. XXXX, XXX, XXX−XXX

$$m_{Li} = (bM_{Li})\frac{S}{V} \quad (4)$$

Here, $\frac{S}{V}$ was defined as the shape factor, which depends on the shape of the LFP nanoparticle. For the LFP samples studied in this work, the particles exhibit a flake structure, as shown in Figure S2A–C. Therefore, the shape factor $\frac{S}{V}$ is $9/r$ for the 42 and 83 nm LFP particles, assuming that LFP particles are cylindrical flakes with a thickness of $2r/9$ or cylindrical rods with an average radius of $2r/9$ and $3/r$ for the nanohollow LFP composite. Because the shape factor is influenced by the particle size, eq 4 can be rewritten as

$$m_{Li} = (bM_{Li})\frac{S}{V} = \frac{9(bM_{Li})}{\sum (d_1y_1 + d_2y_2 + \ldots + d_ny_n)/2} \quad (5)$$

Here, d_n and y_n represent the diameter of the particle and the corresponding percentage of the particle. On the basis of eq 5 and the size distribution of 42 and 83 nm LFP particles (Figure S2B and D), the excess capacity of Li is about 26.2 and 17.6 mA h g^{-1}, respectively. Thus, the excess capacity of LFP-E can exceed the theoretical capacity by 15.4% and 10.3% for 42 and 83 nm particles, respectively.

We then investigated the change in the electronic structure of LFP particles after coating them with GP. The densities of states (DOS) of LFP (010) and the LFP/GP system were shown in Figure S21. For comparison, the total DOS of bulk LFP and the $FePO_4$ system are shown in Figures S22–S23. The calculated band gap of bulk LFP is 3.75 eV, narrower than the experimental value (4.0 eV), as DFT always underestimates the band gap.[28] The electronic structure of LFP (010) is quite similar to that of bulk LFP, which is consistent with previous studies. The wide band gap of the LFP (010) surface occurs because the DOS peak is largely above the Fermi level from the surface Fe atoms. It is noteworthy that surface and bulk have a quite wide band gap, which is not conducive to electron transport, and show semiconductor behavior. The total DOS of the LFP/GP structure in Figure S21B with no band gap around the Fermi level shows conductor behavior, which is obviously an improvement over LFP, as it is important for the LIB application. The nonzero DOS peak around the Fermi level of the LFP/GP structure suggests that the extremely high conductivity of GP is not obviously undermined by the interaction between GP and LFP, and the LFP/GP structure is still quite conductive. Here, GP provides an electronic conductive channel for the LFP/GP structure to improve the electrochemical performance. The much higher conductivity of the LFP/GP structure relative to LFP indicates that the internal resistance of the LFP/GP structure should be much lower, in good agreement with the experimental results.

■ ASSOCIATED CONTENT

Supporting Information

The Supporting Information is available free of charge on the ACS Publications website at DOI: 10.1021/acs.nanolett.7b02315.

Details of structure and morphology; details of electrochemical performance; HRTEM images for the samples; XPS results; Raman spectra; electrochemical kinetics numerical simulations; soft-XAS results; ab initio calculated results (PDF)

Excess Li-ion storage on nanocrystal reconstructed surface to boost battery performance (AVI)

$LiFePO_4$ crystal with reconstructed surface (AVI)

Surface Fe^{2+} supported by soft-XAS and DFT calculations (AVI)

Size-dependent excess capacity in reconstructed $LiFePO_4$ (AVI)

■ AUTHOR INFORMATION

Corresponding Author

*E-mail: panfeng@pkusz.edu.cn.

ORCID

Zonghai Chen: 0000-0001-5371-9463

Chong-Min Wang: 0000-0003-3327-0958

Jun Lu: 0000-0003-0858-8577

Khalil Amine: 0000-0001-9206-3719

Feng Pan: 0000-0002-8216-1339

Author Contributions

Y.D., B.Z., J.Z., and J.H. contributed equally to this work. Y.D. and F.P. conceived and designed the experiments. J.H., J.W., D.J.M., P.Y., T.L., H.G., Z.Z., C.L., H.T., and R.T. performed the experiments. B.Z., J.Z., and X.S. performed the theory calculation. W.L. performed the CV fitting. Z.C., Y.R., Y.L., W.Y., C.-M.W., L.-W.W., J.L., and K.A. analyzed and discussed the results. Y.D., B.Z., and J.Z. wrote the manuscript with the help of L.-W.W. and F.P.

Notes

The authors declare no competing financial interest.

■ ACKNOWLEDGMENTS

The research was financially supported by the National Project for EV Batteries (20121110, Optimum Nano, Shenzhen), National Distinguished Young Scientists of China (51425301), STCSM (12JC1401200), Guangdong Innovation Team Project (no. 2013N080), Natural Science Foundation of Guangdong Province (2015A030310138), and Shenzhen Science and Technology Research Grant (nos. ZDSY20130331145131323, CXZZ20120829172325895, JCYJ20120614150338154). Additionally, we acknowledge the support of the ShenZhen National Super Computing Center. The high resolution transmission electron microscopy was accomplished in the Center for Nanoscale Materials at Argonne National Laboratory, a DOE-BES Facility, supported under contract no. DEAC02-06CH11357 by UChicago Argonne, LLC. The Advanced Light Source is supported by the Director, Office of Science, Office of Basic Energy Sciences, of the U.S. Department of Energy under contract no. DE-AC02-05CH11231. L.-W. W. was supported by the Assistant Secretary for Energy Efficiency and Renewal Energy under the Battery Material Research (BMR) program.

■ REFERENCES

(1) Ma, L.; Hendrickson, K. E.; Wei, S.; Archer, L. A. *Nano Today* **2015**, *10*, 315–338.

(2) Zhang, Q. F.; Uchaker, E.; Candelaria, S. L.; Cao, G. Z. *Chem. Soc. Rev.* **2013**, *42*, 3127–3171.

(3) Wang, H.; Dai, H. *Chem. Soc. Rev.* **2013**, *42*, 3088–3113.

(4) Liu, H.; Strobridge, F. C.; Borkiewicz, O. J.; Wiaderek, K. M.; Chapman, K. W.; Chupas, P. J.; Grey, C. P. *Science* **2014**, *344*, 1480.

(5) Kang, B.; Ceder, G. *Nature* **2009**, *458*, 190–193.

(6) Zheng, J.; Hou, Y.; Duan, Y.; Song, X.; Wei, Y.; Liu, T.; Hu, J.; Guo, H.; Zhuo, Z.; Liu, L.; Chang, Z.; Wang, X.; Zherebetskyy, D.;

DOI: 10.1021/acs.nanolett.7b02315
Nano Lett. XXXX, XXX, XXX–XXX

Fang, Y.; Lin, Y.; Xu, K.; Wang, L. W.; Wu, Y.; Pan, F. *Nano Lett.* **2015**, *15*, 6102−6109.
(7) Zhao, Y.; Peng, L.; Liu, B.; Yu, G. *Nano Lett.* **2014**, *14*, 2849−2853.
(8) Wang, L.; Zhou, F.; Meng, Y. S.; Ceder, G. *Phys. Rev. B: Condens. Matter Mater. Phys.* **2007**, *76*, 165435.
(9) Gibot, P.; Casas-Cabanas, M.; Laffont, L.; Levasseur, S.; Carlach, P.; Hamelet, S.; Tarascon, J.-M.; Masquelier, C. *Nat. Mater.* **2008**, *7*, 741−747.
(10) Xu, G.; Liu, Z.; Zhang, C.; Cui, G.; Chen, L. *J. Mater. Chem. A* **2015**, *3*, 4092−4123.
(11) Oh, S. M.; Myung, S. T.; Park, J. B.; Scrosati, B.; Amine, K.; Sun, Y. K. *Angew. Chem., Int. Ed.* **2012**, *51*, 1853−1856.
(12) Sun, Y. K.; Oh, S. M.; Park, H. K.; Scrosati, B. *Adv. Mater.* **2011**, *23*, 5050−5054.
(13) Sun, C.; Rajasekhara, S.; Goodenough, J. B.; Zhou, F. *J. Am. Chem. Soc.* **2011**, *133*, 2132−2135.
(14) Zhang, P.; Wang, Y.; Lin, M.; Zhang, D.; Ren, X.; Yuan, Q. *J. Electrochem. Soc.* **2012**, *159*, A402−A409.
(15) Yamada, A.; Chung, S. C.; Hinokuma, K. *J. Electrochem. Soc.* **2001**, *148*, A224−A229.
(16) Franger, S.; Le Cras, F.; Bourbon, C.; Rouault, H. *Electrochem. Solid-State Lett.* **2002**, *5*, A231−A233.
(17) Vu, A.; Stein, A. *Chem. Mater.* **2011**, *23*, 3237−3245.
(18) Wang, Y.; Wang, Y.; Hosono, E.; Wang, K.; Zhou, H. *Angew. Chem., Int. Ed.* **2008**, *47*, 7461−7465.
(19) Hu, L.-H.; Wu, F.-Y.; Lin, C.-T.; Khlobystov, A. N.; Li, L.-J. *Nat. Commun.* **2013**, *4*, 1687.
(20) Liu, X.; Liu, J.; Qiao, R.; Yu, Y.; Li, H.; Suo, L.; Hu, Y. S.; Chuang, Y. D.; Shu, G.; Chou, F.; Weng, T. C.; Nordlund, D.; Sokaras, D.; Wang, Y. J.; Lin, H.; Barbiellini, B.; Bansil, A.; Song, X.; Liu, Z.; Yan, S.; Liu, G.; Qjao, S.; Richardson, T. J.; Prendergast, D.; Hussain, Z.; de Groot, F. M. F.; Yang, W. *J. Am. Chem. Soc.* **2012**, *134*, 13708−13715.
(21) Qiao, R.; Dai, K.; Mao, J.; Weng, T. C.; Sokaras, D.; Nordlund, D.; Song, X.; Battaglia, V. S.; Hussain, Z.; Liu, G.; Yang, W. *Nano Energy* **2015**, *16*, 186−195.
(22) Yang, W.; Liu, X.; Qiao, R.; Olalde-Velasco, P.; Spear, J. D.; Roseguo, L.; Pepper, J. X.; Chuang, Y. D.; Denlinger, J. D.; Hussain, Z. *J. Electron Spectrosc. Relat. Phenom.* **2013**, *190*, 64−74.
(23) Hu, J.; Li, W.; Duan, Y.; Cui, S.; Song, X.; Liu, Y.; Zheng, J.; Lin, Y.; Pan, F. *Adv. Energy Mater.* **2017**, *7*, 1601894.
(24) Kresse, G.; Furthmüller, J. *Phys. Rev. B: Condens. Matter Mater. Phys.* **1996**, *54*, 11169−11186.
(25) Blöchl, P. E. *Phys. Rev. B: Condens. Matter Mater. Phys.* **1994**, *50*, 17953−17979.
(26) Perdew, J. P.; Chevary, J. A.; Vosko, S. H.; Jackson, K. A.; Pederson, M. R.; Singh, D. J.; Fiolhais, C. *Phys. Rev. B: Condens. Matter Mater. Phys.* **1992**, *46*, 6671−6687.
(27) Howard, W. F.; Spotnitz, R. M. *J. Power Sources* **2007**, *165*, 887−891.
(28) Xiao, H.; Tahir-Kheli, J.; Goddard, W. A. *J. Phys. Chem. Lett.* **2011**, *2*, 212−217.

DOI: 10.1021/acs.nanolett.7b02315
Nano Lett. XXXX, XXX, XXX−XXX